

Analysis of Transitional and Turbulent Flow Through the FDA Benchmark Nozzle Model Using Laser Doppler Velocimetry

JOSHUA O. TAYLOR,^{1,2} BRYAN C. GOOD,¹ ANTHONY V. PATERNO,¹ PRASANNA HARIHARAN,³ STEVEN DEUTSCH,^{1,2} RICHARD A. MALINAUSKAS,³ and KEEFE B. MANNING^{1,4}

¹Department of Biomedical Engineering, The Pennsylvania State University, 205 Hallowell Building, University Park, PA 16802, USA; ²Applied Research Laboratory, The Pennsylvania State University, State College, PA, USA; ³Office of Science and Engineering Laboratories, Food and Drug Administration, Silver Spring, MD, USA; and ⁴Department of Surgery, The Penn State College of Medicine, Hershey, PA, USA

(Received 27 January 2016; accepted 15 June 2016; published online 27 June 2016)

Associate Editor Ajit P. Yoganathan oversaw the review of this article.

Abstract—Transitional and turbulent flow through a simplified medical device model is analyzed as part of the FDA's Critical Path Initiative, designed to improve the process of bringing medical products to market. Computational predictions are often used in the development of devices and reliable *in vitro* data is needed to validate computational results, particularly estimations of the Reynolds stresses that could play a role in damaging blood elements. The high spatial resolution of laser Doppler velocimetry (LDV) is used to collect two component velocity data within the FDA benchmark nozzle model. Two flow conditions are used to produce flow encompassing laminar, transitional, and turbulent regimes, and viscous stresses, principal Reynolds stresses, and turbulence intensities are calculated from the measured LDV velocities. Axial velocities and viscous stresses are compared to data from a prior inter-laboratory study conducted with particle image velocimetry. Large velocity gradients are observed near the wall in the nozzle throat and in the jet shear layer located in the expansion downstream of the throat, with axial velocity changing as much as 4.5 m/s over 200 μm . Additionally, maximum Reynolds shear stresses of 1000–2000 Pa are calculated in the high shear regions, which are an order of magnitude higher than the peak viscous shear stresses (<100 Pa). It is important to consider the effects of both viscous and turbulent stresses when simulating flow through medical devices. Reynolds stresses above commonly accepted hemolysis thresholds are measured in the nozzle model, indicating that hemolysis may occur under certain flow conditions. As such, the presented turbulence quantities from LDV, which are also available for download at <https://fdacfd.nci.nih.gov/>,

provide an ideal validation test for computational simulations that seek to characterize the flow field and to predict hemolysis within the FDA nozzle geometry.

Keywords—Laser Doppler velocimetry, Particle image velocimetry, Turbulence, Reynolds stress, Hemolysis.

INTRODUCTION

Due to an aging population and the increased effectiveness and safety of current medical devices, the use of blood-contacting devices in patients is on the rise.³⁰ Consequently, many companies are attempting to develop faster and more efficient ways to bring new devices to market. One of the most widely used techniques to evaluate devices is computational fluid dynamics (CFD), due to its ability to quickly simulate device performance under a wide range of flow conditions and device geometries (compared with manufacturing prototypes and testing them *in vitro* or *in vivo*). CFD is routinely used in the development and analysis of a variety of medical devices, including ventricular assist devices,^{9,17,28,32,38,39,50,53,56,57} prosthetic heart valves,^{14,15,19,42} stents,^{22,31,43} and filters^{2,16,52}; unfortunately, CFD predictions of biological responses to devices, such as hemolysis and thrombosis, are limited. This is primarily due to the representation of complex biological phenomena as simplified mathematical models and to the lack of comprehensive fluid mechanics and blood damage benchmark datasets to validate CFD simulations for transitional and turbulent flow through three-dimensional geometries relevant to medical devices. In an

Address correspondence to Keefe B. Manning, Department of Biomedical Engineering, The Pennsylvania State University, 205 Hallowell Building, University Park, PA 16802, USA. Electronic mail: kbm10@psu.edu

attempt to rectify the latter, the Food and Drug Administration (FDA) has partnered with academia and industry to study flow *in vitro* and *in silico* through a simplified medical device model, the FDA nozzle model, as part of its “Critical Path Initiative” (CPI).²⁷ The FDA launched the CPI in 2004 in an effort to improve test methodologies and processes that could bring new and safer medical products to patients more quickly.

One goal of this FDA inter-laboratory study is to provide researchers and device developers with a benchmark model to assess CFD-based predictions of hemolysis in blood-contacting devices. As blood damage is partly dependent upon the fluid dynamics through devices, accurate *in vitro* and *in silico* quantification of flow fields encompassing laminar, transitional, and turbulent regimes is necessary. Initially, three independent laboratories used particle image velocimetry (PIV) to collect velocity data in the FDA nozzle for laminar, transitional, and turbulent flow regimes.²¹ In general, the measured velocities among laboratories differed by around 10%; however, velocity differences of up to 60% were found in the reattachment region for the transitional flow condition.

Using the same FDA nozzle geometry, researchers from 28 independent groups participated in a CFD study to determine the variability in and accuracy of simulation results when only general guidelines on the computational methods were provided. Stewart *et al.*⁵¹ found considerable variability among the computational results from the groups, even though they all were using the same flow conditions. Differences were largely the result of turbulence models underestimating centerline velocities in laminar regions and inaccurately predicting velocities and shear stresses in regions of flow separation. The simulation results were compared to the PIV results of Hariharan *et al.*²¹ to determine accuracy.

While PIV is an excellent technique for globally investigating mean velocity profiles, including the jet and near-wall flows that are relevant to the study of blood-contacting devices,^{34,40,41,45} improved spatial and temporal resolution is needed to accurately calculate turbulent, or Reynolds, stresses, which could play a role in hemolysis⁴⁷ and platelet activation.⁶ Laser Doppler velocimetry (LDV) is a point measurement technique with the necessary spatial and temporal accuracy to resolve turbulent fluctuations,²⁹ and LDV has often been used to study flow through medical devices when turbulence is expected, including in stents,¹³ ventricular assist devices,^{3–5,11,44} and prosthetic heart valves.^{24,33,35–37,48,55} Furthermore, direct comparisons of LDV and PIV measurements found the largest disagreements in high shear regions⁴⁶ and in the calculations of turbulence quantities,⁸ leading to the assertion that the integration of PIV and LDV tech-

niques is the most efficient way to characterize the flow fields of medical devices.²⁹

In an effort to complement the PIV²¹ and CFD⁵¹ studies of the FDA nozzle model, LDV is used to acquire velocity measurements in the same geometry and under the same flow conditions. The LDV velocities can be used to calculate turbulence quantities, such as Reynolds stresses and turbulence intensities (TIs), while also providing estimates of viscous and wall shear stresses. The LDV results, when combined with those from PIV, will provide researchers with a comprehensive data set with which to validate their experimental and computational methods and will help to improve computational approaches for resolving turbulent and transitional flow through the geometric features present in the FDA nozzle model.

METHODS

Flow Loop

The FDA acrylic nozzle model is used in this study (Fig. 1a), and Hariharan *et al.*²¹ document details of the machining process, surface characteristics, and dimension tolerances. The model consists of inlet and outlet regions of equal diameter ($= 12$ mm) and a throat region ($D = 4$ mm) between them. One transition from 12 to 4 mm is sudden, while the other is gradual. The model is used in two downstream flow orientations: sudden expansion (SE) or conical diffuser (CD) at the exit of the throat section, with 12 cross sections in each orientation being investigated, as displayed in Figs. 1b and 1c, respectively. Additionally, two lines aligned with the axial dimension of the model in the SE orientation are studied, a center line ($r = 0$ mm) and a line extending axially from the throat wall (“ledge line” at $r = 2$ mm), to better characterize the fluid dynamics downstream of the sudden expansion (Fig. 1b).

To ensure complete bubble removal from the nozzle, the model is incorporated into one of two vertical flow loop configurations depending on whether it is used in the SE (Fig. 2a) or CD (Fig. 2b) orientation. The loop configurations are the same as those of Hariharan *et al.*,²¹ and flow loop details are repeated here for convenience. Acrylic extenders and stainless steel pipes ($D = 12$ mm for both) are attached to both ends of the model. With these extensions, the entrance region in both orientations is approximately 120 cm long, or 100 times the pipe diameter, which ensures fully developed and axially aligned flow at the model inlet. The elongated exit region, approximately 100 cm for both orientations, minimizes outlet flow effects within the model. In both flow orientations, a stagna-

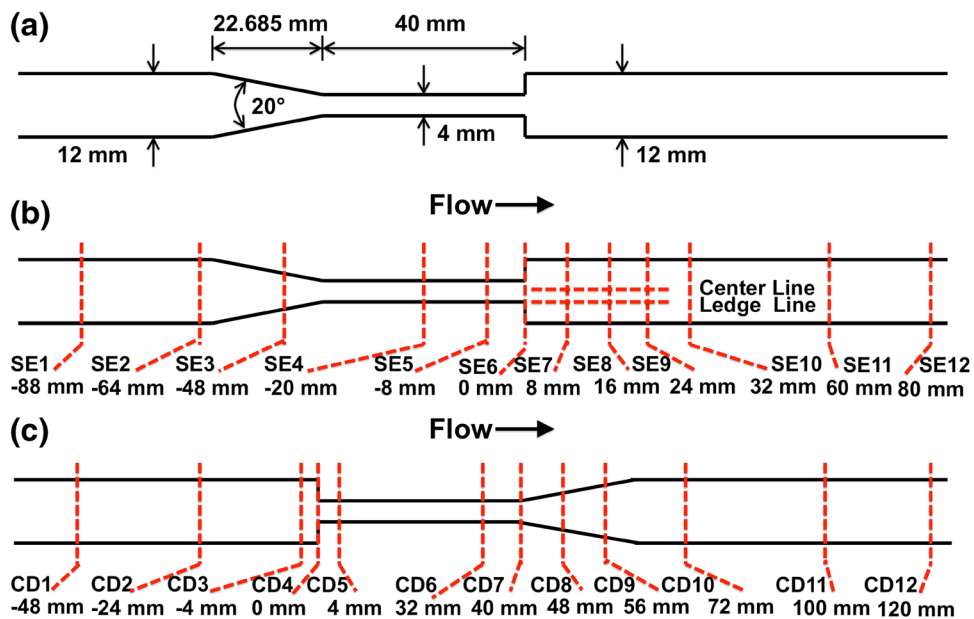


FIGURE 1. (a) Dimensions of the FDA nozzle geometry. (b) Cross sections for data collection in the SE orientation, in which the model consists of a conical concentrator followed by a sudden expansion. Also illustrated are the center and ledge lines downstream of the sudden expansion. (c) Cross sections for data collection in the CD orientation, in which the model consists of a sudden contraction followed by a conical diffuser.

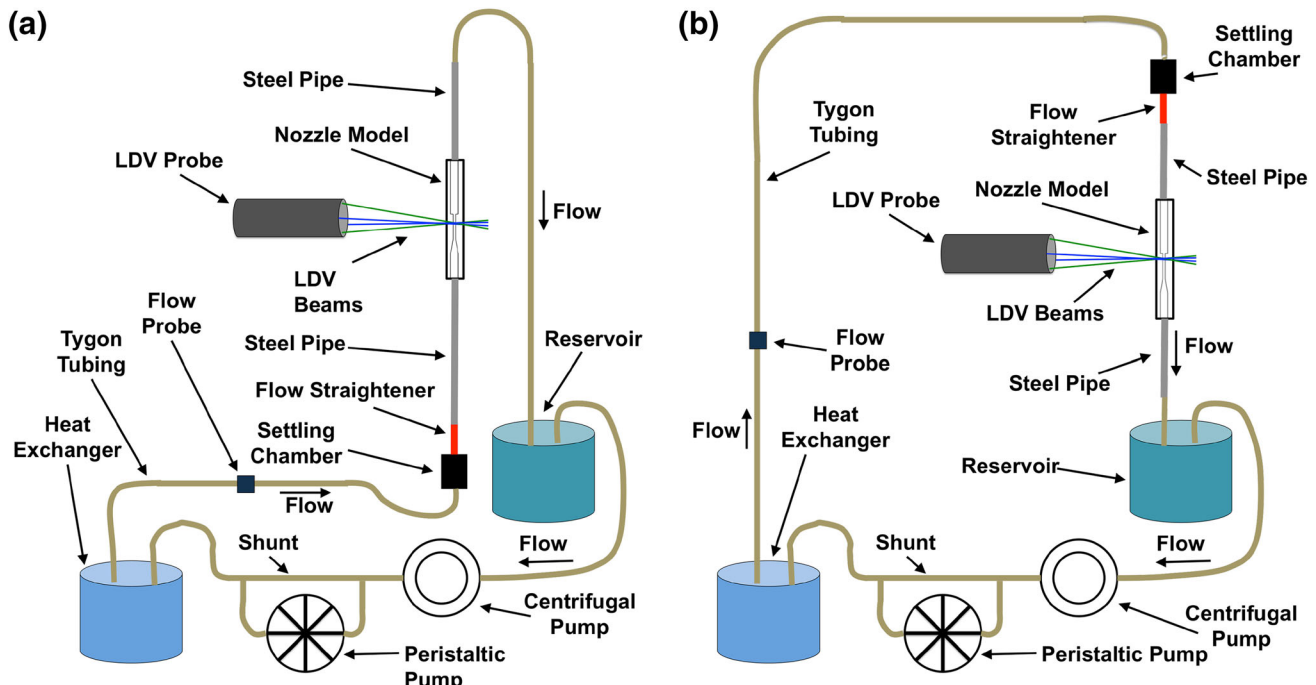


FIGURE 2. Flow loop configuration for (a) SE and (b) CD orientations. Flow direction is indicated with arrows, and loop components are not drawn to scale. In (a) and (b), the peristaltic pump is only used for loop filling and draining, and flow moves through the shunt during data collection.

tion chamber and flow straightener (comprised of thirteen 0.25 cm diameter tubes arranged in a bundle and aligned co-axially) are placed in series on the upstream side of the entrance region (120 cm upstream of

the acrylic model). The stagnation chamber decelerates and mixes the incoming fluid, while the flow straightener removes any remaining disturbances and asymmetries in the flow.

A Newtonian blood analog fluid composed of 50/30/20 wt% sodium iodide (NaI)/water/glycerol is used in the flow loop. The analog fluid is formulated to match the refractive index of the acrylic nozzle model (1.49) and to have a kinematic viscosity of 3.9 cSt, measured at 22 °C using a viscometer (Vilastic Scientific, Inc., Austin, TX). It is important to match the refractive index of the fluid to the refractive index of the model to ensure the model and fluid appear optically homogenous to the incident LDV beams. A kinematic viscosity is chosen that matches the fluid viscosity of a previous PIV study²¹ in the same geometry. The temperature of the fluid is maintained at 22 ± 0.5 °C using a heat exchanger (Thermo Scientific, Waltham, MA, USA) in the flow loop to minimize viscosity changes during data collection. The experimental standard operating procedure (SOP) is identical to the SOP used in the PIV nozzle model study.²¹

The flow loop is initially primed using a peristaltic pump (Cole-Parmer, Vernon Hills, IL, USA), and, after filling, the peristaltic pump is essentially removed from the flow loop using a shunt (see Fig. 2). The fluid is driven through the loop during data collection by a centrifugal pump (Cole-Parmer, Vernon Hills, IL, USA) placed upstream of the model. The pump is placed upstream, rather than downstream, of the model to prevent regions of low pressure and cavitation in the model. The pump is used to produce two constant flow rates (1.47 and 3.68 LPM) through the nozzle model, corresponding to throat Reynolds numbers (Re) of 2000 and 5000, respectively (calculated using the throat diameter, the average velocity in the throat region, and the kinematic viscosity of the blood analog). The flow rate is monitored with a flow probe (Transonic Systems, Ithaca, NY, USA) and verified by integrating collected velocity profiles over the model cross section. Using these two flow rates allows velocity data to be collected in laminar, transitional, and turbulent flow regimes.

Hariharan *et al.*²¹ provide uncertainties associated with the acrylic model dimensions (less than 1%), fluid properties (less than 5%), and Reynolds number (less than 10%) within their detailed error analysis of the experimental SOP.

Laser Doppler Velocimetry

A two component LDV system (TSI, Shoreview, MN, USA)^{24,35,36} is used to collect velocity data within the nozzle model. An argon-ion laser beam is split into pairs of green (514.5 nm) and blue (488 nm) beams, and a 135 mm focal length lens converges the two sets of beams into an elliptic probe volume with dimensions of approximately 35 μm × 35 μm × 275 μm in the blood analog fluid. The LDV system is manipulated

such that the two short dimensions of the probe volume, along which velocity measurements are collected, are aligned with the axial and radial axes of a cylindrical coordinate system. Due to the axisymmetric nature of the model, the circumferential velocity component is ignored. A Bragg cell shifts the frequency of one beam from each pair by 40 MHz, creating a moving interference, or fringe, pattern in the probe volume. The LDV system is operated in back scatter mode, with the receiving fiber inside the transmitting probe, and the blood analog fluid is seeded with hollow glass beads (Potters Industries, Inc., Valley Forge, PA, USA). The diameter ($d_p = 10\mu\text{m}$) and density ($\rho_p = 2.5\text{g/cm}^3$) of the tracer particles yield a particle relaxation time, τ_p , of approximately 2 μs , which can be used to calculate a Stokes number ($S_k = \tau_p U/L$) of approximately 2.5×10^{-3} at the Re5000 condition. From a practical standpoint, particle tracing errors in turbulent flow are less than 1% when $S_k < 0.1$.⁵⁴ Twelve cross sections in each orientation and at each flow condition are selected for velocity data collection (Figs. 1b and 1c), which match those of previous PIV and CFD studies using the same geometry.^{21,51} At each cross section, velocity is measured every 200 μm across the diameter of the model, with 10,000 realizations at each spatial location. The velocity measurements are collected using software coincidence and a 100% gate scale setting. This ensures a two-dimensional velocity vector is only recorded if both velocity components are collected within the same burst window (tens of microseconds). The same procedure is used to collect velocities along the center and ledge lines.

The spatial resolution of the LDV is half of the probe volume, or approximately 17.5 μm along the short axes and 137.5 μm along the long axis. Furthermore, a maximum data rate of 100 kHz for the FSA 4000 signal processor (TSI, Shoreview, MN, USA) corresponds to a temporal resolution of 10 μs . The placement of the transmitting probe relative to the model is manipulated to produce a spatial resolution of 17.5 μm in the plane of data collection, corresponding to the axial and radial components of velocity. Finally, there is an additional 1% uncertainty associated with all velocity measurements due to minor software miscalculations of the fringe spacing.²³

Data Processing

Before any calculations or analyses are performed with the raw velocity data, the data set is filtered to remove outliers. The velocity components are referred to as u and v , which represent the axial and radial components of velocity, respectively. A filtering tech-

nique based on one proposed by Baldwin⁵ is implemented using MATLAB (The MathWorks, Natick, MA, USA) at each data location. An ellipse, centered on the mean velocity components for the specific location in the model and with axis lengths equal to multiples of the respective standard deviations, is used to determine which velocity measurements are removed from the data set. A 4.5 standard deviation filter is used, as this removes approximately 1% of the velocity data from each location (leaving approximately 9900 velocity measurements out of the initial 10,000). The ellipse is aligned with the axes of the principal Reynolds normal stresses by rotating the ellipse by the angle calculated using Eq. (1).

$$\theta = \frac{1}{2} \tan^{-1} \left[\frac{2(\bar{\rho}u'v')}{(\bar{\rho}u'u') - (\bar{\rho}v'v')} \right] \quad (1)$$

In Eq. (1), $\bar{\rho}u'u'$, $\bar{\rho}v'v'$, and $\bar{\rho}u'v'$ are two components of the Reynolds normal stress (RNS) and the Reynolds shear stress (RSS), respectively, and are calculated in Eqs. (2)–(4), where u' and v' are the fluctuating components of velocity (such that $u = U + u'$, where U is the mean velocity), ρ is the fluid density, and N is the total number of velocity measurements at that spatial location.

$$\bar{\rho}u'u' = \rho \sum_{n=1}^N \frac{(u')^2}{N} \quad (2)$$

$$\bar{\rho}v'v' = \rho \sum_{n=1}^N \frac{(v')^2}{N} \quad (3)$$

$$\bar{\rho}u'v' = \rho \sum_{n=1}^N \frac{(u')(v')}{N} \quad (4)$$

The two velocity components are rotated by the angle from Eq. (1), as shown in Eq. (5). The filter removes any velocity vectors that do not satisfy the condition of Eq. (6), where u'_{rotated} and v'_{rotated} are the rotated velocity fluctuations, and $s_{u,\text{rotated}}$ and $s_{v,\text{rotated}}$ are the standard deviations of the rotated velocity fluctuations. Figure 3 illustrates the filter for one example location.

$$\begin{bmatrix} \cos\theta & \sin\theta \\ -\sin\theta & \cos\theta \end{bmatrix} \begin{bmatrix} u' \\ v' \end{bmatrix} = \begin{bmatrix} u'_{\text{rotated}} \\ v'_{\text{rotated}} \end{bmatrix} \quad (5)$$

$$\left(\frac{u'^2_{\text{rotated}}}{(4.5 \cdot s_{u,\text{rotated}})^2} \right) + \left(\frac{v'^2_{\text{rotated}}}{(4.5 \cdot s_{v,\text{rotated}})^2} \right) < 1 \quad (6)$$

During the filtering process, the experimental velocities are scaled using Re similarity, Eq. (7).

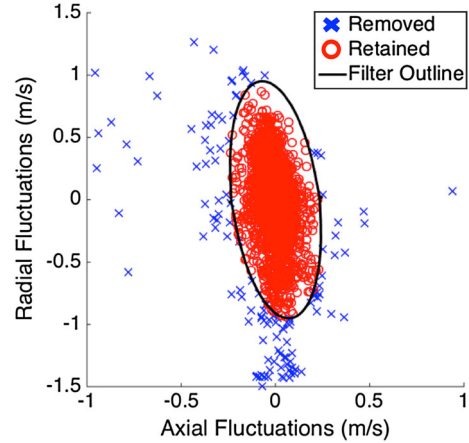


FIGURE 3. Visualization of the filter used to remove outliers from the LDV data. The ellipse (black line) is centered on the mean axial and radial velocity, and it has been rotated to align with the principal Reynolds stresses. At this example location, 1.26% of the collected velocities are removed.

$$U_{\text{blood}} = U_{\text{NaI}} \times \frac{v_{\text{blood}}}{v_{\text{NaI}}} \quad (7)$$

The LDV data are scaled to allow for accurate comparisons between the LDV and previous CFD⁵¹ and PIV²¹ results. The CFD study modeled blood as a Newtonian fluid with a dynamic viscosity of 3.5 cP and a density of 1056 kg/m³,⁵¹ and thus a kinematic viscosity (v) of 3.314 cSt. The PIV study also scaled the measured velocities using the CFD viscosity.²¹ In Eq. (7), v_{NaI} is 3.9 cSt, v_{blood} is 3.314 cSt, and U_{NaI} is the collected LDV velocity. The scaled velocity, U_{blood} , is presented in the rest of this manuscript for velocity profiles, Reynolds stresses, and turbulence intensities. After the velocities at every location are scaled and filtered, new means and standard deviations are calculated for the axial and radial velocity components. Additionally, the principal Reynolds stresses (PRS, $\sigma_{1,2}$) and maximum Reynolds shear stress (MRSS, τ_{\max}), Eqs. (8) and (9), respectively, along with the relative axial and radial TIs, Eqs. (10) and (11), respectively, are calculated.

$$\sigma_{1,2} = \frac{(\bar{\rho}u'u') + (\bar{\rho}v'v')}{2} \pm \sqrt{\left[\frac{(\bar{\rho}u'u') - (\bar{\rho}v'v')}{2} \right]^2 + (\bar{\rho}u'v')^2} \quad (8)$$

$$\tau_{\max} = \sqrt{\left[\frac{(\bar{\rho}u'u') - (\bar{\rho}v'v')}{2} \right]^2 + (\bar{\rho}u'v')^2} \quad (9)$$

$$TI_u = \frac{\sqrt{\sum_{n=1}^N \frac{(u')^2}{N}}}{U_{\text{throat,avg}}} \quad (10)$$

$$TI_v = \frac{\sqrt{\sum_{n=1}^N \frac{(v')^2}{N}}}{U_{\text{throat,avg}}} \quad (11)$$

In Eqs. (8) and (9), $\overline{pu'}$, $\overline{pv'}$, and $\overline{pu'v'}$ are calculated using Eqs. (2)–(4), respectively. In Eqs. (10) and (11), N represents the number of velocity measurements at a location, and $U_{\text{throat,avg}}$ is the scaled, average velocity in the throat region (a different constant for each Re). Using $U_{\text{throat,avg}}$ instead of U to normalize the TI values allows for consistent comparisons between all locations and cross sections for each Re, as using U would have biased the TI values at near wall locations with low average velocities. Finally, the viscous shear stress (ϵ) is calculated at every cross section using Eq. (12), where μ is the dynamic viscosity of blood used in the CFD study (3.5 cP).⁵¹

$$\epsilon = \mu_{\text{blood}} \frac{U_j - U_{j+1}}{d} \quad (12)$$

U_j and U_{j+1} are mean axial velocities at adjacent measurement locations, and d is the distance between them. Additionally, Eq. (12) is used to estimate the wall shear stress (WSS) at each cross section by assuming the surface-normal velocity gradient is linear near the wall. For the WSS calculations, the velocities at the nearest measurement location to the wall on both sides of the model (two WSS estimates at each cross section) are used for U_j ($d = 0.2$ mm), and U_{j+1} is the velocity at the wall, defined as 0 m/s. Due to a combination of the uncertainty associated with velocity measurements, wall location, and Re, the minimum uncertainty associated with the LDV WSS calculation is roughly 20%; however, the uncertainty increases as the assumption of a linear near-wall velocity profile becomes less valid.

Furthermore, raw PIV data are taken from Hariharan *et al.*²¹ for calculation of WSS. The PIV WSS values are calculated using in-house MATLAB code based on the technique developed by Hochareon *et al.*,²⁶ in which four PIV interrogation regions that intersect the wall (two upstream and two downstream of the desired cross-section) are used to estimate the WSS at the cross section of interest. A WSS is calculated for each interrogation region using Eq. (12), and they are averaged to provide a single WSS estimate for one side of the model. Similarly, four interrogation regions are used on the opposite side of the model for a second WSS estimate. In contrast to LDV, the distance, d , from U_j to the wall varies for each interrogation region. Due to partial occlusion of the interrogation regions by the acrylic wall, a centroid-shift algorithm is used to accurately

calculate the distance between the near-wall PIV velocity vector and the model wall.

The LDV velocities and viscous shear stresses are presented with the previous PIV results from our research group, Lab-2 from Hariharan *et al.*,²¹ but velocities along the center and ledge lines and all turbulence statistics (Reynolds stresses and turbulence intensities) are only presented for LDV.

RESULTS

Inlet Velocity Comparisons to Theoretical Values

To ensure flow is fully developed as it entered this test section, the most upstream cross sections (SE1 and CD1) are compared to the theoretical fully developed profiles calculated using the appropriate flow rate (Fig. 4). The experimental results from both LDV and PIV agree with the theoretical profiles for both flow conditions and orientations. The maximum velocities measured with both techniques are within 3.5% of the

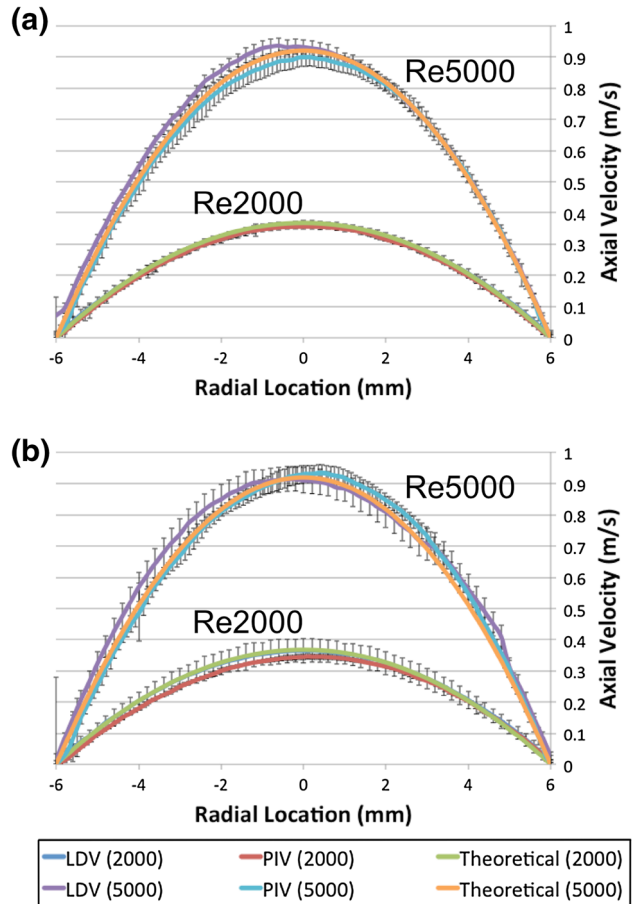


FIGURE 4. LDV and PIV axial velocity profiles at (a) SE1 and (b) CD1 compared to theoretical profiles for fully developed flow. Both flow conditions are displayed, and error bars for the experimental curves denote standard deviations.

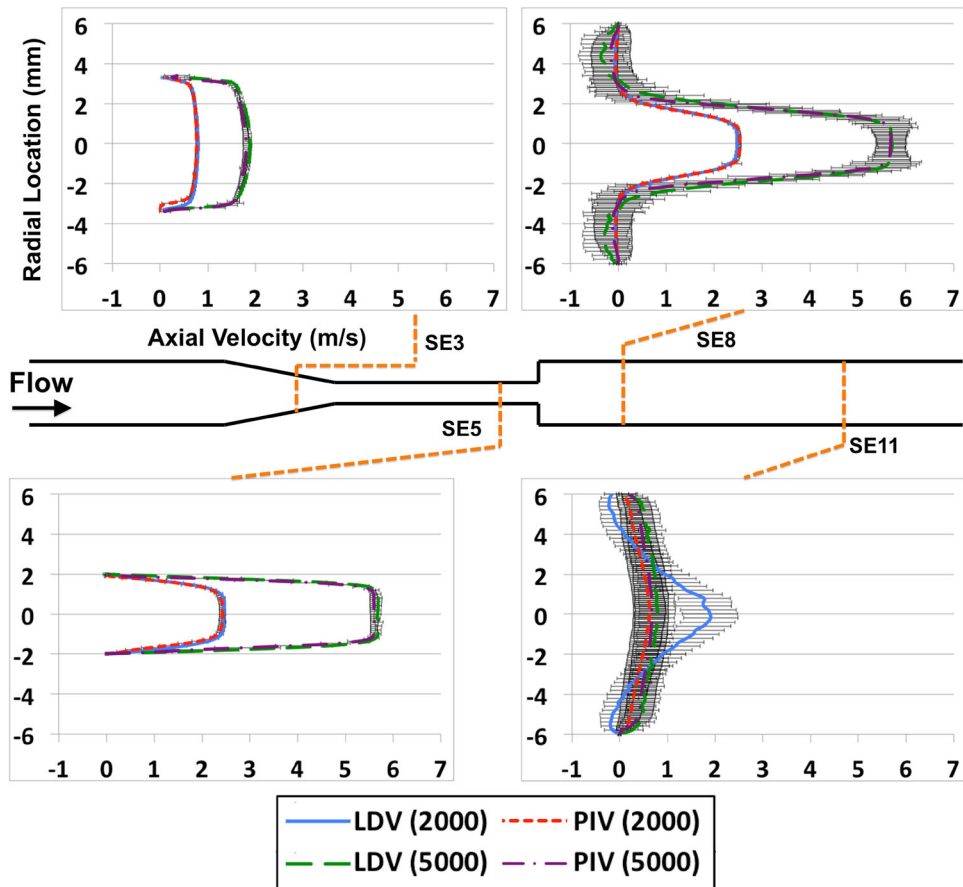


FIGURE 5. Axial velocity profiles collected using LDV and PIV for select cross sections. (3, 5, 8, and 11) in the SE orientation. Both flow conditions are plotted in each graph, and error bars represent the standard deviations. In each plot, the horizontal axis displays axial velocity (m/s), and the vertical axis displays radial location (mm)—see the SE3 plot.

theoretical values, except for the PIV profile in the CD-2000 condition (6%). Similarly, the largest percent error when comparing PIV maximum velocities to the LDV maximum velocities at CD1 occurs in the Re2000 condition (5.4%). Additionally, the LDV profiles at SE1 and CD1 are integrated over the model cross section to verify the measured flow rates. The integrated flow rates for the Re2000 condition closely match those measured with the flow probes, with percent errors of 0.4 and 1.0% in the SE and CD orientations, respectively. However, larger discrepancies are calculated in the Re5000 condition, with percent errors of 4.3 and 7.6%, respectively. Radial velocities are near zero (<0.015 m/s) at SE1 and CD1 for both flow conditions.

Axial Velocity

Axial velocity profiles for both flow conditions and orientations are presented in Figs. 5 and 6. The displayed cross sections (four for each orientation) are selected to provide representative velocity profiles for

each section of the test model and to illustrate similarities and differences between the LDV and PIV data sets.

Sudden Expansion Cross Sections

Beginning with the SE orientation (Fig. 5), the velocity profile is blunted when it enters the conical concentrator (SE3), and the centerline velocities are approximately double what they are in the upstream region (SE1 in Fig. 4a). In the throat region (SE5), the profiles remain blunted, and the centerline velocities rapidly increase (to ~ 2.5 m/s for Re2000 and ~ 5.5 m/s for Re5000) as flow adjusts to the smaller model diameter. Downstream of the sudden expansion, a jet forms with centerline velocities similar to those in the throat and flow separates from the wall, leading to reverse flow in near-wall regions (SE8). The velocity fluctuations in the shear layer between the jet core and the separated flow are large in the Re5000 condition, as shown with standard deviations around 1 m/s at radial locations of $\pm 2\text{--}2.4$ mm (compared with standard

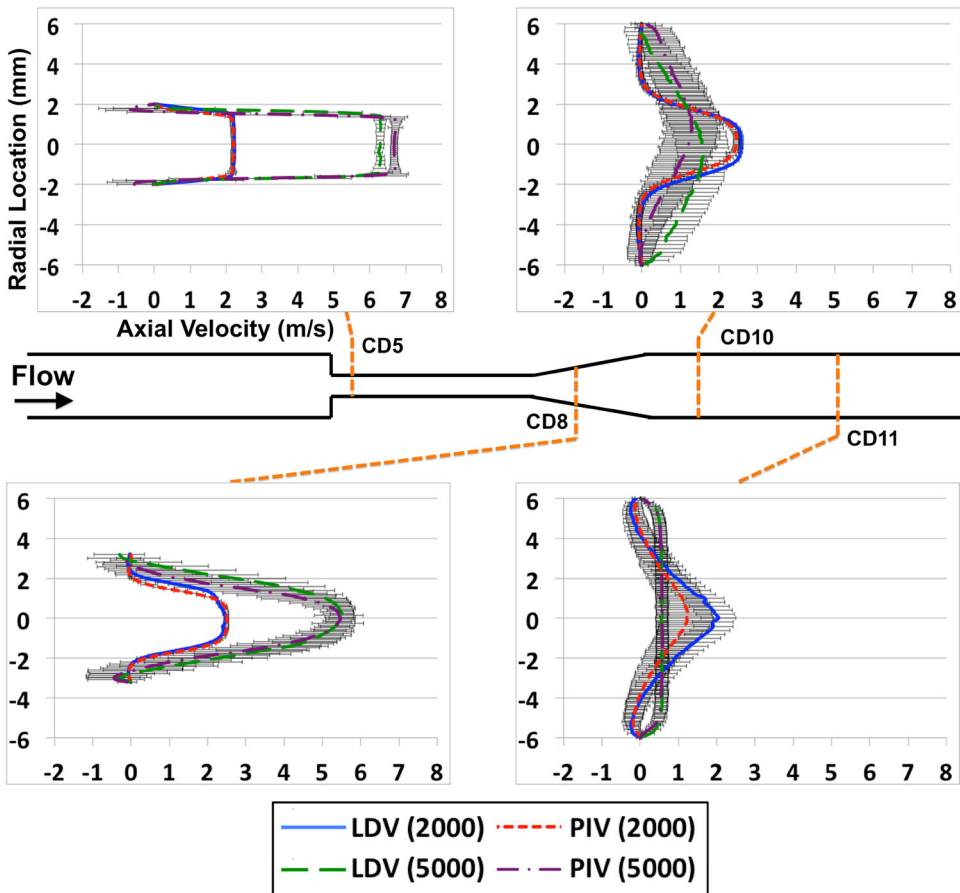


FIGURE 6. Axial velocity profiles collected using LDV and PIV for select cross sections (5, 8, 10, and 11) in the CD orientation. Both flow conditions are plotted in each graph, and error bars represent the standard deviations. In each plot, the horizontal axis displays axial velocity (m/s), and the vertical axis displays radial location (mm)—see the CD5 plot.

deviations of 0.3–0.5 m/s near $r = 0$). Finally, the jet core is either partly (Re2000) or completely (Re5000) broken down by SE11. Flow has reattached at Re5000, and the profile is slightly blunted with centerline velocities near 0.8 m/s. At Re2000, however, flow has not reattached by SE11, and centerline velocities remain high—approximately 2 m/s. The flow instabilities in this region also lead to large standard deviations, approaching 0.6 m/s near the centerline. This is the only cross section and flow condition where sizeable differences are observed between the PIV and LDV mean velocity profiles in the SE orientation (PIV centerline velocities at Re2000-SE11 are approximately 0.6 m/s with standard deviations of about 0.3 m/s, and flow has reattached). The LDV measurements show reattachment by SE12 (not shown), and the discrepancy between LDV and PIV centerline velocities decrease to a factor of two at SE12: 0.6 and 0.3 m/s, respectively. Similar discrepancies in the measured reattachment length were found between experiments and labs during our previous inter-laboratory PIV study.²¹

Conical Diffuser Cross Sections

In the CD orientation (Fig. 6), flow proceeds into the throat region through a sudden contraction. The velocities collected downstream of the contraction (CD5) show a blunted profile with large velocity gradients between the throat wall and center. The LDV centerline velocities are approximately 2.3 and 6.3 m/s at Re2000 and Re5000, respectively, but there is disagreement between LDV and PIV data at Re5000-CD5, with PIV measuring slightly higher centerline velocities (~6.7 m/s) and standard deviations in the high shear regions (~25% greater than LDV near $r = \pm 1.8$ mm). When flow in the conical diffuser is examined (CD8), small amounts of flow recirculation are found near the walls and the jet velocity profiles are more rounded than those observed downstream of the throat in the SE orientation (Fig. 5). Flow is unstable at Re5000-CD8 (Fig. 6), manifested as large standard deviations (~1.3 m/s at $r = \pm 2.5$ mm) compared to the mean flow (~1 m/s at $r = \pm 2.5$ mm). The unstable jet at Re5000 has broken down and flow has reattached by CD10; although, large standard devia-

tions are still calculated across the model diameter (0.5–0.7 m/s) compared to the mean velocities (largely between 0.5 and 1.5 m/s). Additionally, some asymmetry is observed in the velocity profiles, with both the LDV and PIV profiles showing maximum velocity at off center locations, -0.4 and 0.75 mm, respectively. Asymmetry in the mean velocity profiles is likely caused by disturbances generated at the edge of the expansion and amplified in the downstream shear layers.¹⁰ At Re2000-CD10, flow remains separated from the wall, and centerline velocities are approximately equal to their values in the throat and conical diffuser, with small standard deviations (≤ 0.12 m/s). A small amount of recirculation is still found at CD11, but standard deviations increase to between 0.4 and 0.55 m/s across the majority of the model diameter due to instabilities caused by jet breakdown. Similar to the region of jet breakdown in the SE orientation at Re2000 (SE11 in Fig. 5), LDV measured higher centerline velocities than PIV: 2 vs. 1.25 m/s. Flow is attached, and the LDV and PIV profiles are again in agreement at CD12 (not shown). The profiles at Re5000-CD11 are blunt with mean velocities of approximately 0.55 m/s across the model diameter.

Axial Lines

The normalized axial velocities along the center and ledge lines (Fig. 7) provide additional insight into the jet behavior downstream of the sudden expansion and allow for comparisons to literature. Again, the center line is collected at a constant radial location of 0 mm, and the ledge line is collected at a constant radial location of 2 mm. Figure 7a shows normalized centerline axial velocity is essentially constant at nearly 1.5 for up to $7D_{\text{throat}}$ downstream of the sudden expansion at Re2000, while the normalized axial velocity along the ledge line rises from about 0.35 to a little over 0.65, with standard deviations for both lines around 0.025. In contrast, centerline axial velocity remains constant at 1.35 until about $5.5D_{\text{throat}}$ downstream of the sudden expansion at Re5000, when the velocity decreases quickly to 1.1 over the next $1.5D_{\text{throat}}$ (Fig. 7b). Moreover, the standard deviations at Re5000 rise from approximately 0.02 to 0.25 over the length of the centerline, from the beginning ($z/D_{\text{throat}} = 0.4$) to the end ($z/D_{\text{throat}} = 7$). The ledge line axial velocity increases from 0.35 to 0.75 over the line, while the standard deviations again increase by an order of magnitude, from 0.025 to 0.28.

Laminar Stress

Viscous Shear Stress

The viscous shear stress is estimated from the mean LDV and PIV velocities using Eq. (12). Figures 8 and 9

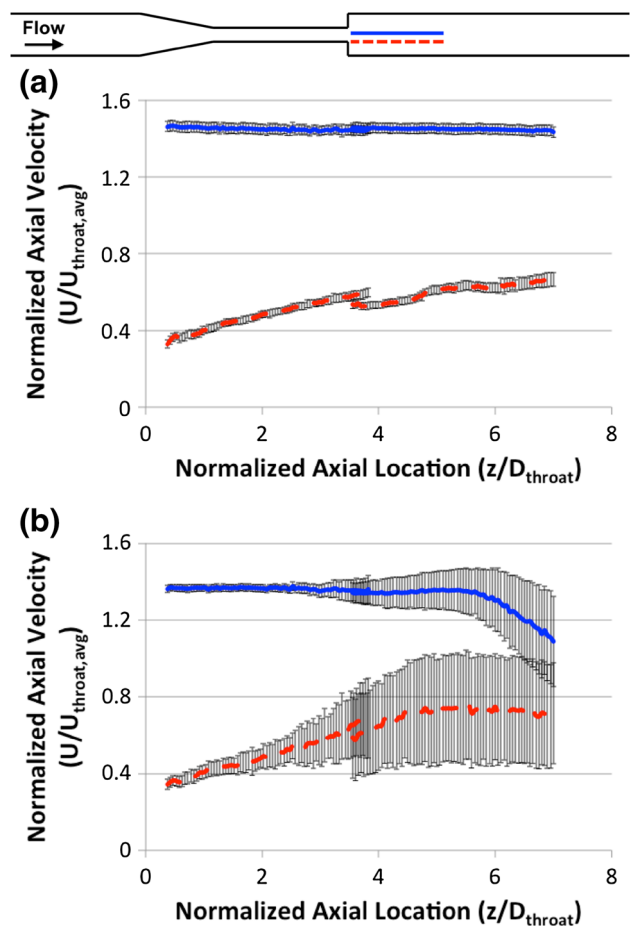


FIGURE 7. Normalized axial velocity plotted along the center (solid) and ledge (dashed) lines in the SE orientation at (a) Re2000 and at (b) Re5000. Normalized axial location denotes the distance downstream of the sudden expansion (scaled using the throat diameter), and error bars represent standard deviation. Due to LDV traverse constraints, the center and ledge lines were each collected in two parts, which can be seen overlapping near a normalized location of 3.75. The ledge lines show a slight mismatch between the two axial velocity profiles—approximately 10% for both Re. In (a), the mismatch is likely a combination of uncertainty and variability in the velocity measurements (standard deviations are ~4% of the mean) and spatial errors (half of the LDV probe volume) introduced when traversing to the ledge line location. Similarly, in (b), the 10% mismatch is primarily caused by the variability in the velocity measurements (standard deviations are ~30% of the mean) and uncertainty in the spatial location.

display viscous shear stress profiles at the same representative cross sections used in Figs. 5 and 6, respectively. Peak stresses are calculated in both orientations in the throat region, where large velocity gradients are found near the walls: approximately 50 Pa in the SE orientation (SE5 in Fig. 8) and 100 Pa in the CD orientation (CD5 in Fig. 9) at Re5000. At Re2000, viscous shear stresses are 20–30% of the Re5000 values at SE5 and CD5. Downstream of the throat (SE8 and CD8), peaks in the viscous stress profile in both orientations are calculated near radial locations of ± 2 mm, where large

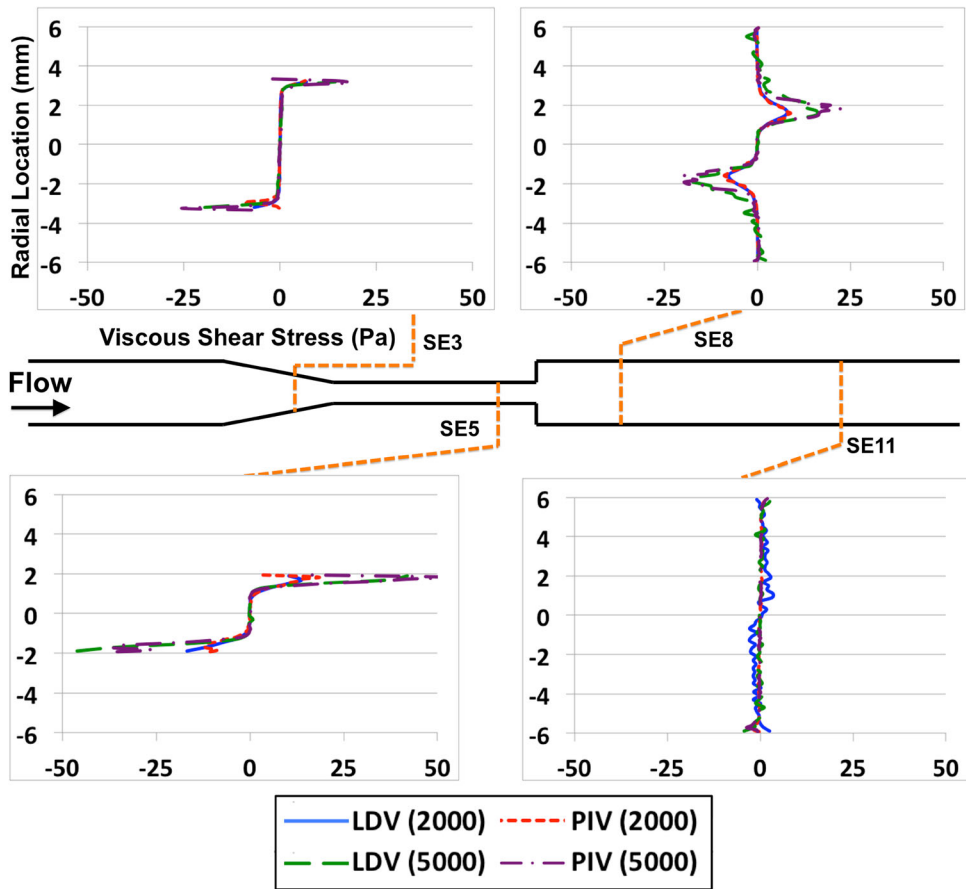


FIGURE 8. Viscous shear stress profiles calculated using LDV and PIV velocities for select cross sections (3, 5, 8, and 11) in the SE orientation. In each plot, the horizontal axis displays shear stress (Pa), and the vertical axis displays radial location (mm)—see the SE3 plot.

velocity gradients are found between the throat jet and separated flow. The peaks correspond to shear stresses of approximately 10 Pa at Re2000 and 20 Pa at Re5000 for both orientations. As the jet spreads and flow reattaches, viscous shear stresses drop to 5 Pa or less at both flow conditions and orientations.

Wall Shear Stress

As WSS is often an important metric to consider when investigating hemolysis and thrombosis in medical devices, WSSs are presented at each cross section examined in the LDV and PIV studies (Fig. 10). In general, the LDV and PIV estimates of WSS display similar trends, but there is some disagreement between the peak viscous stresses in Figs. 8 and 9 (often occurring near the wall) and the WSSs in Fig. 10. These discrepancies can partly be traced to the fact that two different techniques (described in the Methods section) are used to calculate PIV fluid viscous stress and WSS.

Upstream of the throat section (SE1, SE2; CD1–CD3) for all conditions, mean WSS are less than 1.5 Pa (Fig. 10). The largest WSS for both flow conditions and Re is in the throat region, with peak LDV WSS reaching 15.6 and 52 Pa at SE4 for Re2000 (Fig. 10a) and for Re5000 (Fig. 10c), respectively. Similarly, peak LDV WSS of 20 and 61.5 Pa are calculated in the throat region at Re2000 (Fig. 10b) and at Re5000 (Fig. 10d) in the CD orientation. Many of the LDV and PIV WSS estimates in the throat are presented with large standard deviations, with some standard deviations exceeding the mean value. Downstream of the throat, mean WSS at Re2000 are all below 5 Pa in magnitude, and mean WSS at Re5000 are all less than 15 Pa in magnitude (Fig. 10).

Additionally, WSSs upstream of the throat (SE1, SE2; CD1, CD2) are compared with theoretical values calculated by assuming a fully developed profile to check for accuracy. None of them show a statistically significant difference at the $p = 0.05$ level when compared to the theoretical values calculated by assuming a parabolic inlet profile.

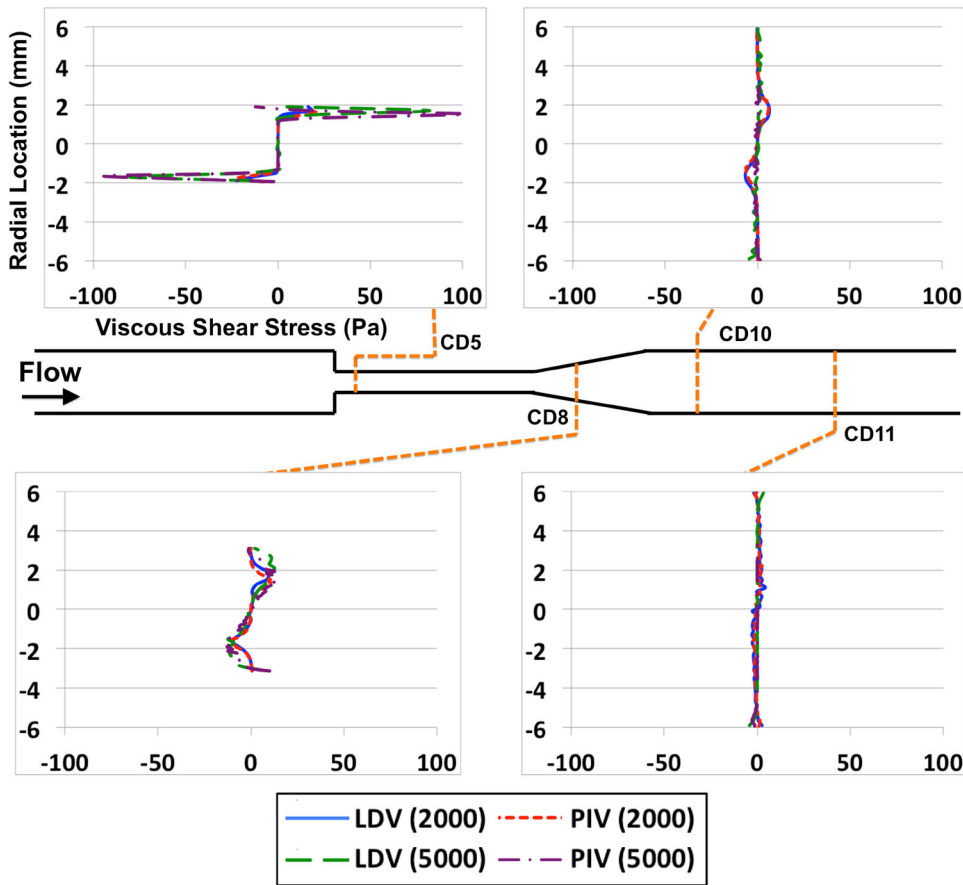


FIGURE 9. Viscous shear stress profiles calculated using LDV and PIV velocities for select cross sections (5, 8, 10, and 11) in the CD orientation. In each plot, the horizontal axis displays shear stress (Pa), and the vertical axis displays radial location (mm)—see the CD5 plot.

Turbulence Statistics

Sudden Expansion and Conical Diffuser Cross Sections

The turbulence statistics are plotted for every cross section in Fig. 11 (PRS and MRSS) and Fig. 12 (TI). There is no appreciable turbulence at cross sections upstream of the throat region (SE1–SE3; CD1–CD3) under any considered flow conditions, as all stresses are below 6 Pa and all TI are below 0.025. One exception is the near wall measurement ($r = -6$ mm) in CD1 at the Re2000 condition, where noise artificially increased the turbulence statistics.

The throat region in the SE orientation (SE4–SE6) also produces little turbulence, with all MRSS less than 20 Pa (Fig. 11a) and all TI below 0.05 (Fig. 12a). The throat region in the CD orientation (CD4–CD7) showed small amounts of turbulence at Re2000 (all Reynolds stresses less than 35 Pa and all TI less than 0.09); however, the largest turbulence statistics calculated in the entire study are found in the CD throat region at Re5000. Specifically, CD5 in the Re5000 condition has peak PRS and MRSS of 4650 and

2000 Pa, respectively (Fig. 11b), and peak axial and radial TI of 0.37 and 0.22, respectively (Fig. 12b). Peak Reynolds stresses about one quarter of those at CD5 and turbulence intensities about one half of those at CD5 are calculated at CD6 and CD7.

Regions downstream of the throat (SE7–SE12; CD8–CD12) show considerable turbulence in both orientations, but the cross sections of peak turbulence differ between the Re2000 and Re5000 conditions. The maximum Reynolds stresses and TI in the model at Re2000 are calculated at SE11 and CD11 and are due to the breakdown of the jet. The peak PRS and MRSS in the SE/CD orientations are approximately 635/555 and 240/210 Pa, respectively (Fig. 11), and the peak axial and radial TI are approximately 0.36/0.33 and 0.22/0.22, respectively (Fig. 12). Turbulence is decreased by SE12 and CD12 at Re2000, as peak PRS and MRSS drop to about 220/45 and 70/10 Pa, respectively (Fig. 11), and axial and radial TI decline to 0.21/0.10 and 0.13/0.08, respectively (Fig. 12). The highest turbulence quantities downstream of the throat at Re5000 first occur in the shear layer around the

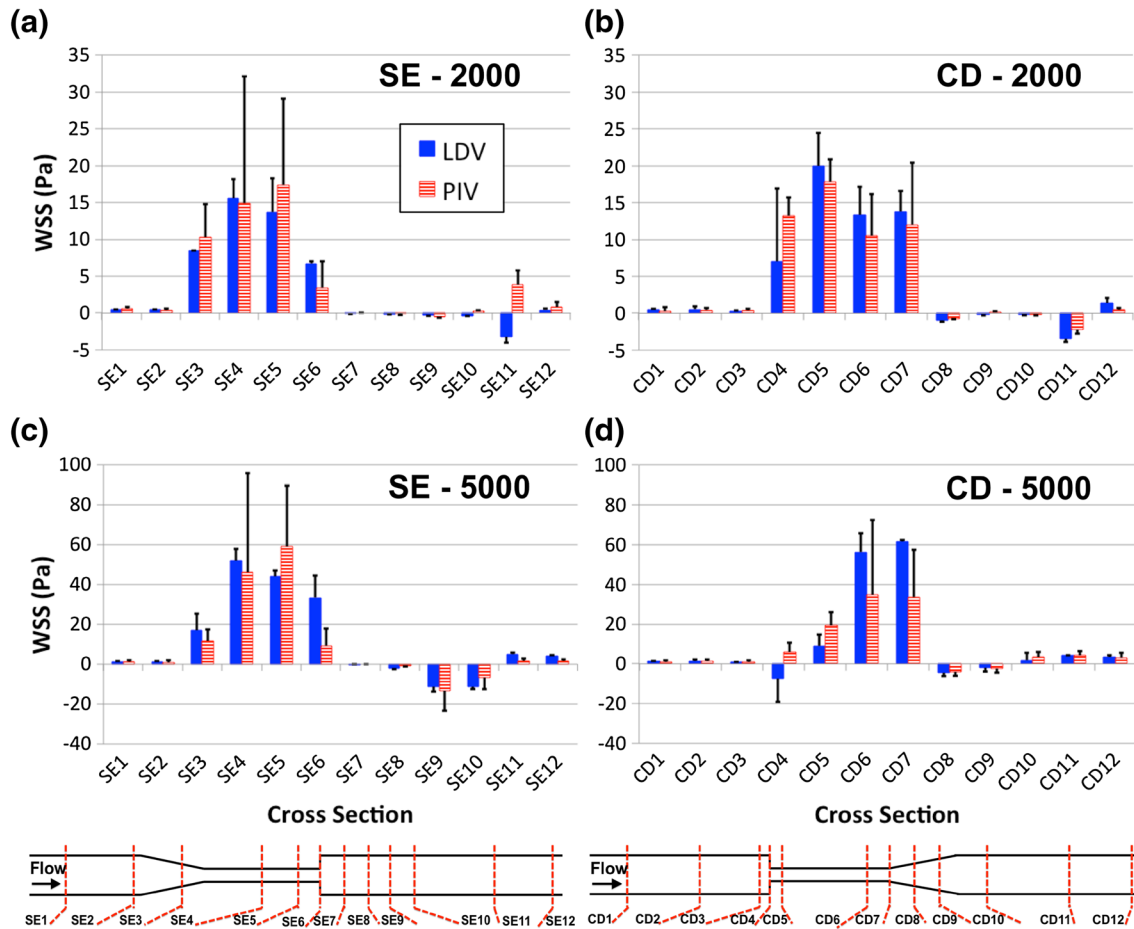


FIGURE 10. WSS calculated using LDV and PIV velocities at every cross section: (a) Re2000 in the SE orientation, (b) Re2000 in the CD orientation, (c) Re5000 in the SE orientation, and (d) Re5000 in the CD orientation. The vertical axes show mean WSS (Pa), while the horizontal axes show model cross section. Error bars represent the standard deviation ($n_{LDV} = n_{PIV} = 2$: one WSS estimate from each side of the model).

throat jet (SE8 and SE9; CD8) and are characterized by peak values near $r = \pm 2$ mm. As the jet breaks down, high turbulence quantities are calculated across the model diameter (SE10; CD9 and CD10). Peak PRS and MRSS values in the downstream section of the models for SE/CD orientations are approximately 3350/3600 and 1150/1350 Pa, respectively (Fig. 11), and maximum axial and radial TI are 0.30/0.32 and 0.25/0.24, respectively (Fig. 12). Small amounts of turbulence are still observed at SE11, SE12, CD11, and CD12 at Re5000, but all Reynolds stresses are less than 300 Pa and all TI are less than 0.10.

Axial Lines

To further investigate and characterize the turbulent region downstream of the throat in the SE orientation, normalized MRSS and axial TI for the center and ledge lines at Re5000 are plotted in Fig. 13. MRSS is normalized using the fluid density and the square of the mean throat velocity ($\tau_{max}/\rho_{Nal} U_{throat}^2$), and the

normalized values at Re2000 are not shown, as they are negligible: the peak normalized MRSS and axial TI are approximately 6.5×10^{-4} and 0.04, respectively. At Re5000, the turbulence statistics along the center line begin near zero but approach 0.015 and 0.25 for normalized MRSS (Fig. 13a) and axial TI (Fig. 13b), respectively, at an axial location of $7D_{throat}$. Similarly, the turbulence statistics along the ledge line begin near zero and increase in the axial direction; however, peak values of nearly 0.04 and 0.3 for normalized MRSS (Fig. 13a) and axial TI (Fig. 13b), respectively, are found at an axial location of $4.85D_{throat}$. Downstream of that location, the turbulence statistics decrease to 0.026 for MRSS and 0.26 for TI by an axial location of $7D_{throat}$.

DISCUSSION

We have investigated the fluid mechanics through the FDA nozzle under transitional and turbulent

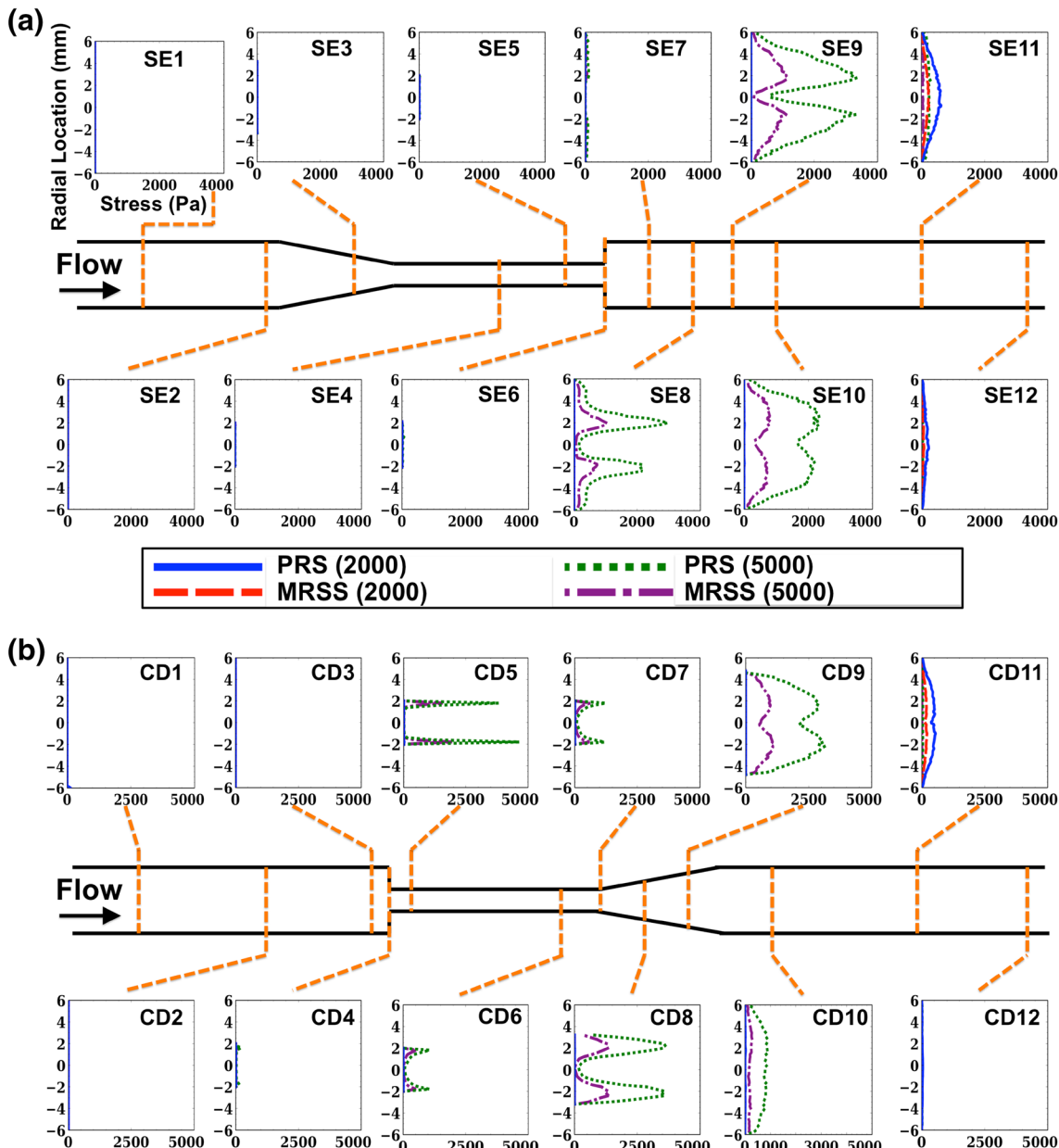


FIGURE 11. PRS and MRSS profiles for all cross sections presented for (a) SE and (b) CD orientations. The horizontal axes (different scales for each orientation) show Reynolds stress (Pa), and the vertical axes show radial location (mm)—see the SE1 plot in (a).

conditions using the high spatial and temporal resolution of LDV to complement a previous PIV study in the same geometry,²¹ and the present study provides a comprehensive evaluation of the Reynolds stresses and TIs in the nozzle model. CFD simulations that endeavor to predict biological responses within the FDA nozzle model, specifically hemolysis and platelet activation, can be compared to the dataset of MRSS calculated in this study using the LDV velocities to ensure congruence. Also, while TIs are not normally used in predictions of hemolysis or platelet activation, they provide a normalized measure of the turbulent velocity

fluctuations that need to be resolved for calculations of Reynolds stresses. The high spatial resolution of LDV in the plane of data collection (an order of magnitude better than PIV) also allows for accurate assessment of the velocities and viscous shear stresses in regions with large velocity gradients, particularly in the throat section.

After following the experimental procedures described by Hariharan *et al.*,²¹ all collected velocity profiles at the model inlet (SE1 and CD1) are consistent with those expected for fully developed pipe flow (Fig. 4). The flow loops for both orientations are de-

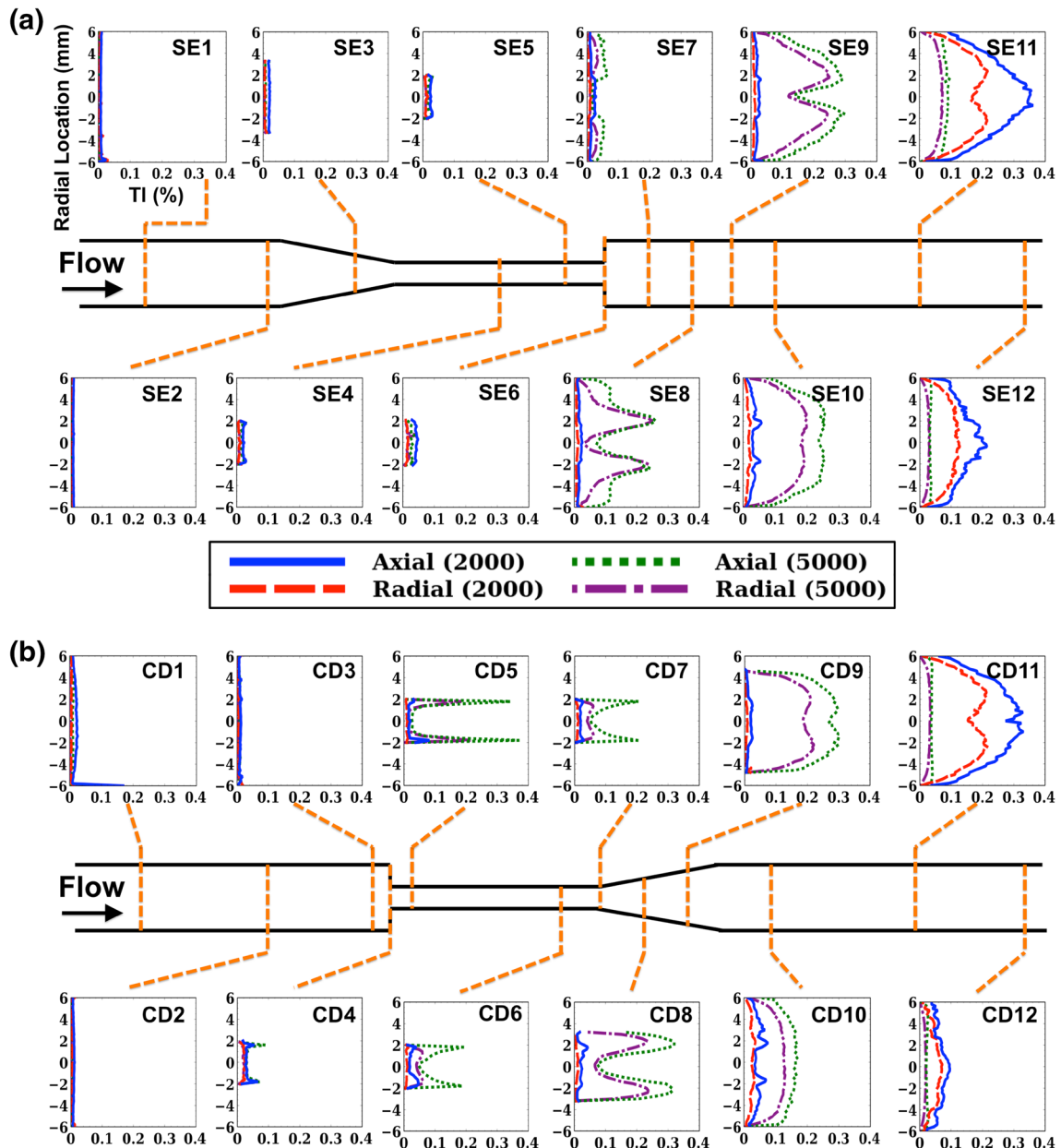


FIGURE 12. Relative axial and radial TI profiles for all cross sections presented for (a) SE and (b) CD orientations. The horizontal axes show TI (%), and the vertical axes show radial location (mm)—see the SE1 plot in (a).

signed to remove all disturbances and asymmetries before flow enters the nozzle model, and the comparisons of experimental velocities to theoretical parabolic profiles ensures this is accomplished. Additionally, all viscous and turbulent stresses at the model inlet are trivial, as expected for laminar flow (the transitional, Re2000, and turbulent, Re5000, conditions are based on the throat Re; whereas, the inlet Re = 667 and 1667, respectively – are laminar for both flow conditions due to the larger inlet diameter).

The throat region is characterized by blunt velocity profiles and high velocity gradients near the walls

(Figs. 5 and 6). The viscous shear stresses are the maximum at the throat region for both flow rates in both directions (Figs. 8 and 9). However, the gradual narrowing of the model in the SE orientation via the conical concentrator lessens the near-wall velocity gradients, and thus the viscous shear stresses, with peak values calculated in the CD near-wall throat region (Fig. 9) roughly double those calculated in the SE throat region (Fig. 8). Similarly, the sudden contraction leading into the CD throat region generates the largest Reynolds stresses and turbulence intensities in the entire study at Re5000-CD5, while the SE throat

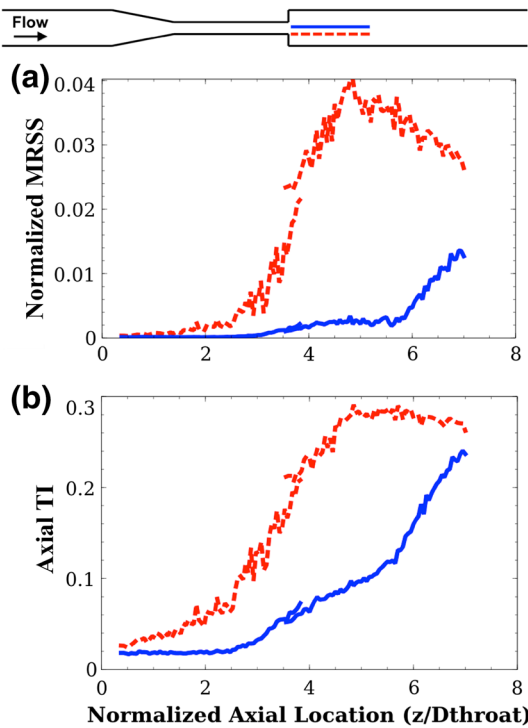


FIGURE 13. (a) Normalized MRSS ($\tau_{\max}/\rho_{\text{Nal}} U_{\text{throat}}^2$) and (b) relative axial TI plotted along the center (solid) and ledge (dashed) lines in the SE orientation at Re5000. Normalized axial location denotes the distance downstream of the sudden expansion (scaled using the throat diameter). Due to LDV traverse constraints, the center and ledge lines were each collected in two parts, which can be seen overlapping near a normalized location of 3.75.

region has turbulent quantities an order of magnitude less at the same flow condition (Figs. 11 and 12).

Again, contrasting geometries are used to transition from the throat to the larger downstream diameter in the SE and CD orientations: a sudden expansion and a conical diffuser, respectively. However, unlike in the throat region, the gradual change in the geometry does not noticeably lessen turbulence as flow decelerates, with similar Reynolds stresses and TIs at SE8, SE9, CD8, and CD9 (Figs. 11 and 12). Flow deceleration can increase the growth rate of shear-layer instabilities,⁴⁹ which helps explain why similar levels of turbulence are found at cross sections downstream of the throat, regardless of whether the expansion is sudden or gradual. The cross section with the most turbulence at Re2000 occurs as the jet from the throat breaks down in the downstream region (SE11 and CD11). It is noteworthy, but not unexpected,^{1,18} that the jet breaks down and flow reattaches further downstream at the Re2000 condition than at the Re5000 condition. This is likely caused by higher energy dissipation at Re5000 (seen in the large turbulent stresses and intensities) at SE8 – SE10 and CD8 – CD10 (Figs. 11 and 12); conversely, turbulent quantities near zero are calculated

for Re2000 at the same planes. Additionally, the normalized turbulence statistics collected along the center and ledge lines at the turbulent condition (Fig. 13) are the same order of magnitude as those expected for a turbulent circular jet.⁷

The peak MRSS calculated in the model are an order of magnitude higher than the peak viscous shear stresses, but we are, unfortunately, unable to convert our presented viscous shear stresses to their maximum values, as was done with Reynolds shear stresses, due to our inability to calculate viscous normal stress in the axial direction from the collected velocity data. This suggests that both viscous and turbulent stresses need to be examined when evaluating flow fields and, furthermore, that principal and maximum stresses should be used, if possible, when discussing the biological impact of turbulent and viscous stresses so the results are not biased by the coordinate system used for data collection. Importantly, hemolysis and platelet activation are not only a function of shear stress magnitude, but also of exposure time and stress history. This makes it difficult to define a threshold stress for either phenomenon; however, estimates are available in the literature for particular situations. One such estimate, from Sallam and Hwang,⁴⁷ was calculated using a turbulent jet, which likely produced exposure times on the same order of magnitude as those in the FDA nozzle model; consequently, their threshold value of 400 Pa gives a rough estimate of the stress levels that might cause hemolysis under the present experimental conditions in the nozzle model. Additionally, a rough estimate of the exposure time in Sallam and Hwang's⁴⁷ experiment can be calculated with their maximum jet velocity and the distance downstream of the jet exit at which their peak RSS was found, which yields an exposure time of 1.4 ms. However, Sallam and Hwang's threshold was presumably underestimated, as they did not work with MRSS, and Grigioni *et al.*²⁰ calculated that it should be closer to 600 Pa. Even though the peak MRSS measured in the FDA nozzle model is two to three times larger (Fig. 11) than the reported threshold value, the FDA's inter-laboratory hemolysis measurements in the nozzle model²⁵ showed minimal levels of hemolysis in both model orientations at Re5000. Since hemolysis is a function of both shear stress and exposure time, a better understanding about the exposure time is required to evaluate the risk of both hemolysis and platelet activation in the nozzle model.

The LDV and PIV axial velocities and viscous shear stresses are plotted together to illustrate the general similarities between the two techniques (see Figs. 5 and 6 and Figs. 8 and 9, respectively). However, there are some key areas where they differ. The largest differences exist in the high velocity gradient regions in the

throat section at Re5000, near the reattachment point downstream of the throat at Re2000 (SE10 and SE11; CD10 and CD11), and in the WSS calculations. Differences in the measurement capabilities of the large near-wall velocity gradients in the throat are quantified by comparing the estimated viscous shear stresses. Percent differences of 7 to 30% are calculated when comparing the peak PIV viscous stresses to the LDV stresses in the SE throat, while percent differences of 2 to 45% are found in the CD throat. The LDV spatial resolution ($\sim 17.5 \mu\text{m}$) is one order of magnitude better than the PIV spatial resolution ($\sim 175 \mu\text{m}$) in the plane of data collection,²¹ which helps to explain different values in the throat. The LDV velocities are measured every $200 \mu\text{m}$ in the radial direction, and mean velocities at adjacent points vary by as much as 4.5 m/s at Re5000-CD5. The PIV interrogation region contains a distribution of velocities, leading to a single mean velocity being calculated that is not representative of the velocities at the boundaries of the interrogation region. This also contributes to large standard deviations associated with the near-wall PIV axial velocities in the throat, which would also likely artificially increase turbulence statistics if the PIV data were used for that purpose. High shear regions are also observed downstream of the throat in both orientations. Velocities change by 0.5 to 1.5 m/s between adjacent LDV measurement locations at Re5000, and it is unlikely that PIV will accurately resolve the turbulence associated with this region unless a better camera, and thus a higher spatial resolution, is used.

A large discrepancy between LDV and PIV is also observed in the axial velocity profiles at Re2000-SE11 (Fig. 5), with the LDV centerline velocity approximately three times higher than the PIV centerline velocity. Furthermore, the LDV profile shows flow reversal near the walls, while the PIV profile shows none. The techniques are in agreement at SE10 (not shown), and both show reattachment lengths within the range established for transitional flow. Hariharan *et al.*²¹ found disagreement within the PIV data from three independent laboratories at the same cross section, orientation, and flow condition and traced the disagreement to minor discrepancies (less than 10%) in the calculated Re, which leads to large differences in reattachment length in the transitional flow case. A discrepancy between LDV and PIV axial velocity profiles is also observed at Re2000-CD11 in Fig. 6, but it is not as pronounced as that observed at Re2000-SE11 in Fig. 5. In this case, the profiles from both techniques show near-wall flow reversal, peaking at -0.25 and -0.18 m/s for LDV and PIV, respectively; however, the LDV results show a higher centerline velocity

than those from PIV: 2.00 vs. 1.25 m/s , respectively. When each velocity profile is integrated over the model cross section at this cross section, the LDV flow rate has a percent error of -5.0% when compared to the flow rate measured with the flow probe, while the percent error from PIV is -26.1% . By the next downstream cross section, though, the calculated error in the LDV flow rate is 13.4% , while the PIV error is 4.9% . Due to the chaotic and slightly asymmetric flow from jet breakdown at CD11 and CD12 for Re2000, integrating velocity profiles to obtain flow rates can be problematic at these locations; nevertheless, velocity histograms overlap substantially between the two data sets at Re2000-CD11, seen by examining the standard deviations associated with the mean velocities (centerline standard deviations of 0.55 and 0.7 m/s for LDV and PIV, respectively).

Finally, large variability is found in the experimental WSS (Fig. 10), and differences exist between the upstream experimental and theoretical WSSs. Even though the differences in inlet WSS between the experimental estimations and the theoretical values are not statistically significant, the percent errors computed when comparing the mean LDV and PIV WSS to the theoretical WSS are between 8 and 40%. This is likely due to lower out-of-plane spatial resolution of both LDV ($\sim 137.5 \mu\text{m}$), due to an elongated probe volume, and PIV ($\sim 500 \mu\text{m}$), due to the light sheet thickness. The experimental axis with low spatial resolution is aligned with the azimuthal axis for both techniques, and axisymmetric flow decreases the impact of the low out-of-plane resolution on the majority of the experimental results. However, near the curved model wall, the low out-of-plane resolution leads to velocities collected over a range of wall distances and can introduce considerable error into WSS calculations. While the LDV spatial resolution in the plane of data collection, which only allows the wall to be found within $\pm 17.5 \mu\text{m}$, and uncertainty in the Re produce our minimum uncertainty of 20% in the LDV WSS, even though the error associated with the LDV velocities is only 1%, non-linear near-wall velocity profiles and low out-of-plane resolution will introduce additional uncertainty. The uncertainty and variability associated with WSS calculations (see Fig. 10) contribute to the observed discrepancies when WSS are compared to the near-wall viscous stresses displayed in Figs. 8 and 9; however, similar trends are still observed between the two data sets, with maximum stresses observed in the throat region in both orientations and at both Re. Furthermore, the near-wall viscous and WSS are the same order of magnitude throughout the model for all considered conditions.

CONCLUSIONS

We have investigated and characterized laminar, transitional, and turbulent flow in a simplified medical device, the FDA nozzle model, using the high spatial and temporal accuracy of LDV. The nozzle model is used in two orientations, which allows for the study of four geometric features that are relevant to medical devices: conical concentrators, conical diffusers, sudden contractions, and sudden expansions. The current LDV study complements PIV²¹ and CFD⁵¹ studies using the same geometry and provides a comprehensive description of the velocities (Figs. 5, 6, and 7), viscous shear stresses (Figs. 8 and 9), principal Reynolds stresses (Figs. 11 and 13A), and relative turbulence intensities (Figs. 12 and 13B) found throughout the model.

At the turbulent flow condition, a sudden contraction in geometry leading to the throat causes substantially higher Reynolds stresses when compared to a gradual contraction. However, the jet shear layer downstream of the throat, regardless of whether it forms in either the sudden or gradual expansion configuration, is associated with high Reynolds stresses. The highest MRSS calculated in the turbulent flow case are between 1000 and 2000 Pa (while peak PRS approach 5000 Pa) and exceed published thresholds for hemolysis^{4,20,47} and platelet activation.¹² Consequently, CFD models should have the capability to accurately resolve both viscous and turbulent stresses when predicting biological responses, such as hemolysis or platelet activation, in medical devices. Together with the PIV²¹ and CFD⁵¹ studies (<https://fdacfd.nci.nih.gov/>), the current LDV study will help modelers validate their computational methods against a comprehensive characterization of the fluid mechanics within an idealized medical device model.

ACKNOWLEDGMENTS

This study was supported by the US Food and Drug Administration's Critical Path Initiative. We would like to thank Dr. Luke Herbertson for reviewing the manuscript and providing valuable comments.

DISCLAIMER

Any mention of commercial products and/or manufacturers does not imply endorsement by the US Department of Health and Human Services.

DISCLOSURES

The authors have no conflicts or disclosures. No human or animal studies were performed as part of this study.

REFERENCES

- ¹Armalys, B. F., F. Durst, J. C. Pereira, and B. Schönung. Experimental and theoretical investigation of backward-facing step flow. *J. Fluid Mech.* 127:473–496, 1983.
- ²Aycock, K. I., R. L. Campbell, K. B. Manning, S. P. Sastry, S. M. Shontz, F. C. Lynch, and B. A. Craven. A computational method for predicting inferior vena cava filter performance on a patient-specific basis. *J Biomech Eng.* 136(8):081003, 2014.
- ³Bachmann, C., G. Hugo, G. Rosenberg, S. Deutsch, A. Fontaine, and J. M. Tarbell. Fluid dynamics of a pediatric ventricular assist device. *Artif. Organs.* 24(5):362–372, 2000.
- ⁴Baldwin, J. T., S. Deutsch, D. B. Geselowitz, and J. M. Tarbell. LDA measurements of mean velocity and Reynolds stress fields within an artificial heart ventricle. *J. Biomed. Eng.* 116(2):190–200, 1994.
- ⁵Baldwin, J. T., S. Deutsch, H. L. Petrie, and J. M. Tarbell. Determination of principal Reynolds stresses in pulsatile flows after elliptical filtering of discrete velocity measurements. *J. Biomed. Eng.* 115(4A):396–403, 1993.
- ⁶Bluestein, D., K. B. Chandran, and K. B. Manning. Towards non-thrombogenic performance of blood recirculating devices. *Ann. Biomed. Eng.* 38(3):1236–1256, 2010.
- ⁷Bradshaw, P., D. H. Ferriss, and R. F. Johnson. Turbulence in the noise-producing region of a circular jet. *J. Fluid Mech.* 19(04):591–624, 1964.
- ⁸Browne, P., A. Ramuzat, R. Saxena, and A. P. Yoganathan. Experimental investigation of the steady flow downstream of the St. Jude bileaflet heart valve: a comparison between laser Doppler velocimetry and particle image velocimetry techniques. *Ann. Biomed. Eng.* 28(1):39–47, 2000.
- ⁹Burgreen, G. W., J. F. Antaki, Z. J. Wu, and A. J. Holmes. Computational fluid dynamics as a development tool for rotary blood pumps. *Artif. Organs.* 25(5):336–340, 2001.
- ¹⁰Cherdron, W., F. Durst, and J. H. Whitelaw. Asymmetric flows and instabilities in symmetric ducts with sudden expansions. *J. Fluid Mech.* 84(01):13–31, 1978.
- ¹¹Chua, L. P., K. S. Ong, G. Song, and W. Ji. Measurements by laser Doppler velocimetry in the casing/impeller clearance gap of a biocentrifugal ventricular assist device model. *Artif. Organs.* 33(4):360–372, 2009.
- ¹²Deutsch, S., J. M. Tarbell, K. B. Manning, G. Rosenberg, and A. A. Fontaine. Experimental fluid mechanics of pulsatile artificial blood pumps. *Annu. Rev. Fluid Mech.* 38:65–86, 2006.
- ¹³Dorn, F., F. Niedermeyer, A. Balasso, D. Liepsch, and T. Liebig. The effect of stents on intra-aneurysmal hemodynamics: *in vitro* evaluation of a pulsatile sidewall aneurysm using laser Doppler anemometry. *Neuroradiology.* 53(4):267–272, 2011.
- ¹⁴Dumont, K., J. Vierendeels, R. Kaminsky, G. Van Nooten, P. Verdonck, and D. Bluestein. Comparison of the hemodynamic and thrombogenic performance of two bileaflet

- mechanical heart valves using a CFD/FSI model. *J. Biomed. Eng.* 129(4):558–565, 2007.
- ¹⁵Dwyer, H. A., P. B. Matthews, A. Azadani, N. Jaussaud, L. Ge, T. S. Guy, and E. E. Tseng. Computational fluid dynamics simulation of transcatheter aortic valve degeneration. *Interact. Cardiovasc. Thorac. Surg.* 9(2):301–308, 2009.
- ¹⁶Fiore, G. B., U. Morbiducci, R. Ponzini, and A. Redaelli. Bubble tracking through computational fluid dynamics in arterial line filters for cardiopulmonary bypass. *ASAIO J.* 55(5):438–444, 2009.
- ¹⁷Fraser, K. H., M. E. Taskin, B. P. Griffith, and Z. J. Wu. The use of computational fluid dynamics in the development of ventricular assist devices. *Med. Eng. Phys.* 33:263–280, 2011.
- ¹⁸Gach, H. M., and I. J. Lowe. Measuring flow reattachment lengths downstream of a stenosis using MRI. *J. Magn. Reson. Imaging.* 12(6):939–948, 2000.
- ¹⁹Ge, L., H. L. Leo, F. Sotiropoulos, and A. P. Yoganathan. Flow in a mechanical bileaflet heart valve at laminar and near-peak systole flow rates: CFD simulations and experiments. *J. Biomech. Eng.* 127(5):782–797, 2005.
- ²⁰Grigioni, M., C. Daniele, G. D'Avenio, and V. Barbaro. A discussion on the threshold limit for hemolysis related to Reynolds shear stress. *J. Biomech.* 32(10):1107–1112, 1999.
- ²¹Hariharan, P., M. Giarra, V. Reddy, S. W. Day, K. B. Manning, S. Deutsch, S. F. Stewart, M. R. Myers, M. R. Berman, G. W. Burgreen, and E. G. Paterson. Multilaboratory particle image velocimetry analysis of the FDA benchmark nozzle model to support validation of computational fluid dynamics simulations. *J. Biomech. Eng.* 133(4):041002, 2011.
- ²²He, Y., N. Duraiswamy, A. O. Frank, and J. E. Moore. Blood flow in stented arteries: a parametric comparison of strut design patterns in three dimensions. *J. Biomech. Eng.* 127(4):637–647, 2005.
- ²³Herbertson, L.H. Evaluation of Fluid Mechanics and Cavitation Generated by Mechanical Heart Valves during Closure Phase. PhD Dissertation. The Pennsylvania State University; 2009.
- ²⁴Herbertson, L. H., S. Deutsch, and K. B. Manning. Near valve flows and potential blood damage during closure of a bileaflet mechanical heart valve. *J. Biomech. Eng.* 133(9):094507, 2011.
- ²⁵Herbertson, L. H., S. E. Olia, A. Daly, C. P. Noatch, W. A. Smith, M. V. Kameneva, and R. A. Malinauskas. Multi-laboratory study of flow-induced hemolysis using the FDA benchmark nozzle model. *Artif. Organs.* 39(3):237–248, 2015.
- ²⁶Hochareon, P., K. B. Manning, A. A. Fontaine, J. M. Tarbell, and S. Deutsch. Wall shear-rate estimation within the 50 cc Penn State artificial heart using particle image velocimetry. *J. Biomech. Eng.* 126(4):430–437, 2004.
- ²⁷FDA's Critical Path Initiative. 2015. <http://www.fda.gov/ScienceResearch/SpecialTopics/CriticalPathInitiative/ucm076689.htm>. Accessed 16 Oct 2015.
- ²⁸Izraelev, V., W. J. Weiss, B. Fritz, R. K. Newswanger, E. G. Paterson, A. Snyder, R. B. Medvitz, J. Cysyk, W. E. Pae, D. Hicks, and B. Lukic. A passively-suspended Tesla pump left ventricular assist device. *ASAIO J.* 55(6):556–561, 2009.
- ²⁹Kini, V., C. Bachmann, A. Fontaine, S. Deutsch, and J. M. Tarbell. Integrating particle image velocimetry and laser Doppler velocimetry measurements of the regurgitant flow field past mechanical heart valves. *Artif. Organs.* 25(2):136–145, 2001.
- ³⁰Kirklin, J. K., D. C. Naftel, R. L. Kormos, L. W. Stevenson, F. D. Pagani, M. A. Miller, J. T. Baldwin, and J. B. Young. The fourth INTERMACS annual report: 4,000 implants and counting. *J. Heart Lung Transpl.* 31(2):117–126, 2012.
- ³¹LaDisa, Jr, J. F., I. Guler, L. E. Olson, D. A. Hettrick, J. R. Kersten, D. C. Warltier, and P. S. Pagel. Three-dimensional computational fluid dynamics modeling of alterations in coronary wall shear stress produced by stent implantation. *Ann. Biomed. Eng.* 31(8):972–980, 2003.
- ³²Legendre, D., P. Antunes, E. Bock, A. Andrade, J. F. Biscegli, and J. P. Ortiz. Computational fluid dynamics investigation of a centrifugal blood pump. *Artif. Organs.* 32(4):342–348, 2008.
- ³³Leo, H. L., H. Simon, J. Carberry, S. C. Lee, and A. P. Yoganathan. A comparison of flow field structures of two tri-leaflet polymeric heart valves. *Ann. Biomed. Eng.* 33(4):429–443, 2005.
- ³⁴Long, T. C., J. J. Pearson, A. C. Hankinson, S. Deutsch, and K. B. Manning. An *in vitro* fluid dynamic study of pediatric cannulae: the value of animal studies to predict human flow. *J. Biomech. Eng.* 134(4):044501, 2012.
- ³⁵Manning, K. B., L. H. Herbertson, A. A. Fontaine, and S. Deutsch. A detailed fluid mechanics study of tilting disk mechanical heart valve closure and the implications to blood damage. *J. Biomech. Eng.* 130(4):041001, 2008.
- ³⁶Manning, K. B., T. M. Przybysz, A. A. Fontaine, J. M. Tarbell, and S. Deutsch. Near field flow characteristics of the Bjork-Shiley Monostrut valve in a modified single shot valve chamber. *ASAIO J.* 51(2):133–138, 2005.
- ³⁷Maymir, J. C., S. Deutsch, R. S. Meyer, D. B. Geselowitz, and J. M. Tarbell. Mean velocity and Reynolds stress measurements in the regurgitant jets of tilting disk heart valves in an artificial heart environment. *Ann. Biomed. Eng.* 26(1):146–156, 1998.
- ³⁸Medvitz, R. B., J. W. Kreider, K. B. Manning, A. A. Fontaine, S. Deutsch, and E. G. Paterson. Development and validation of a computational fluid dynamics methodology for simulation of pulsatile left ventricular assist devices. *ASAIO J.* 53(2):122–131, 2007.
- ³⁹Medvitz, R. B., V. Reddy, S. Deutsch, K. B. Manning, and E. G. Paterson. Validation of a CFD methodology for positive displacement LVAD analysis using PIV data. *J. Biomech. Eng.* 131(11):111009, 2009.
- ⁴⁰Menon, P. G., N. Teslovich, C. Y. Chen, A. Undar, and K. Pekkan. Characterization of neonatal aortic cannula jet flow regimes for improved cardiopulmonary bypass. *J. Biomech.* 46(2):362–372, 2013.
- ⁴¹Nanna, J. C., M. A. Navitsky, S. R. Topper, S. Deutsch, and K. B. Manning. A fluid dynamics study in a 50 cc pulsatile ventricular assist device: influence of heart rate variability. *J. Biomech. Eng.* 133(10):101002, 2011.
- ⁴²Nobili, M., U. Morbiducci, R. Ponzini, C. Del Gaudio, A. Balducci, M. Grigioni, F. M. Montevercchi, and A. Redaelli. Numerical simulation of the dynamics of a bileaflet prosthetic heart valve using a fluid–structure interaction approach. *J. Biomech.* 41(11):2539–2550, 2008.
- ⁴³Pant, S., N. W. Bressloff, A. I. Forrester, and N. Curzen. The influence of strut-connectors in stented vessels: a comparison of pulsatile flow through five coronary stents. *Ann. Biomed. Eng.* 38(5):1893–1907, 2010.
- ⁴⁴Pedersen, N., P. S. Larsen, and C. B. Jacobsen. Flow in a centrifugal pump impeller at design and off-design conditions—part I: particle image velocimetry (PIV) and laser Doppler velocimetry (LDV) measurements. *J. Fluid Eng.* 125(1):61–72, 2003.

- ⁴⁵Roszelle, B. N., M. G. Fickes, S. Deutsch, and K. B. Manning. Visualization of the Penn State pulsatile pediatric ventricular assist device cannulae and change in outlet valve placement. *Cardiovasc Engr Technol.* 2(4):244–252, 2011.
- ⁴⁶Saga, T., H. Hu, T. Kobayashi, S. Murata, K. Okamoto, and S. Nishio. A comparative study of the PIV and LDV measurements on a self-induced sloshing flow. *J. Vis. Jpn.* 3(2):145–156, 2000.
- ⁴⁷Sallam, A. M., and N. H. Hwang. Human red blood cell hemolysis in a turbulent shear flow: contribution of Reynolds shear stresses. *Biorheology.* 21(6):783–797, 1983.
- ⁴⁸Saxena, R., J. Lemmon, J. Ellis, and A. Yoganathan. An *in vitro* assessment by means of laser Doppler velocimetry of the medtronic advantage bileaflet mechanical heart valve hinge flow. *J. Thorac. Cardiovasc. Sur.* 126(1):90–98, 2003.
- ⁴⁹Shtern, V., and F. Hussain. Effect of deceleration on jet instability. *J. Fluid Mech.* 480:283–309, 2003.
- ⁵⁰Song, X., H. G. Wood, and D. Olsen. Computational fluid dynamics (CFD) study of the 4th generation prototype of a continuous flow ventricular assist device (VAD). *J. Biomech. Eng.* 126(2):180–187, 2004.
- ⁵¹Stewart, S. F., E. G. Paterson, G. W. Burgeen, P. Hariharan, M. Giarra, V. Reddy, S. W. Day, K. B. Manning, S. Deutsch, M. R. Berman, and M. R. Myers. Assessment of CFD performance in simulations of an idealized medical device: results of FDA's first computational interlaboratory study. *Cardiovasc. Eng. Technol.* 3(2):139–160, 2012.
- ⁵²Stewart, S. F., R. A. Robinson, R. A. Nelson, and R. A. Malinauskas. Effects of thrombosed vena cava filters on blood flow: flow visualization and numerical modeling. *Ann. Biomed. Eng.* 36(11):1764–1781, 2008.
- ⁵³Throckmorton, A. L., and A. Untaroiu. CFD analysis of a Mag-Lev ventricular assist device for infants and children: Fourth generation design. *ASAIO J.* 54(4):423–431, 2008.
- ⁵⁴Tropea, C., A. L. Yarin, and J. F. Foss. Spring Handbook of Experimental Fluid Mechanics, Vol. 1. New York: Springer Science & Business Media, 2007.
- ⁵⁵Weston, M. W., D. V. LaBorde, and A. P. Yoganathan. Estimation of the shear stress on the surface of an aortic valve leaflet. *Ann. Biomed. Eng.* 27(4):572–579, 1999.
- ⁵⁶Wu, J., B. E. Paden, H. S. Borovetz, and J. F. Antaki. Computational fluid dynamics analysis of blade tip clearances on hemodynamic performance and blood damage in a centrifugal ventricular assist device. *Artif. Organs.* 34(5):402–411, 2010.
- ⁵⁷Yang, N., S. Deutsch, E. G. Paterson, and K. B. Manning. Numerical study of blood flow at the end-to-side anastomosis of a left ventricular assist device for adult patients. *J. Biomech. Eng.* 131(11):111005, 2009.